11th International Symposium on Turbulence and Shear Flow Phenomena (TSFP11)
Southampton, UK, July 30 to August 2, 2019

FLOW DEVELOPMENT OVER AN ISOLATED DROPLET-INSPIRED SHAPE

Xueqing Zhang
Mechanical and Mechatronics Engineering
University of Waterloo
200 University Ave. W,
Waterloo, ON, Canada, N2L 3G1
x634zhan@uwaterloo.ca

Burak A. Tuna
Mechanical and Mechatronics Engineering
University of Waterloo
200 University Ave. W,
Waterloo, ON, Canada, N2L 3G1
buraka.tuna@gmail.com

Serhiy Yarusevych
Mechanical and Mechatronics Engineering
University of Waterloo
200 University Ave. W,
Waterloo, ON, Canada, N2L 3G1
syarus@uwaterloo.ca

Sean D. Peterson
Mechanical and Mechatronics Engineering
University of Waterloo
200 University Ave. W,
Waterloo, ON, Canada, N2L 3G1
peterson@uwaterloo.ca

ABSTRACT

Flow development over isolated surface-mounted, 3D obstacles submerged in a laminar boundary layer is investigated at a Reynolds number based on height of $\mathrm{Re}_h = 2070$ using Particle Image Velocimetry (PIV). The three geometries considered are inspired by morphological configurations of droplets deposited on a flat surface in a crossflow. The mean flow topology and shedding of arch-shaped structures are characterized and compared. The mean streamwise features include a horseshoe vortex system and a base vortex pair, with the latter being formed due to tilting of the arch vortices and inducing central upwash downstream of the obstacle. In the near wake, flow development is largely influenced by the model aspect ratio. In the far wake, the interactions between horseshoe vortices and base vortices lead to the local onset of laminar-to-turbulent transition.

Introduction

Droplet mobility on a surface due to aerodynamic loading is of interest in a wide range of industrial applications, including wing de-icing (Hansman & Turnock, 1989) and surface cleaning (Antonini *et al.*, 2012). However, modeling droplet mobility is hindered by a lack of reliable estimations of aerodynamic forces on representative shapes. In this context, both liquid droplet mobility on the surface, as well as its effect on the ambient flow, are of interest.

The flow over a surface mounted hemisphere, which is of similar shape to a sessile droplet, has been considered in a number of previous investigations (Acarlar & Smith, 1987; Savory & Toy, 1986*a*,*b*; Wood *et al.*, 2016). It has been found that these obstacles can induce a horseshoe vortex system due to boundary layer separation immediately upstream of the obstacle; the arms of the horseshoe vortices wrap around the obstacle and orient predominantly in the streamwise direction downstream of the object (Savory & Toy, 1986*a*). In the near wake, the build-up and subsequent release of vorticity on the obstacle surface leads to periodic shedding of large-scale arch vortices (Acarlar & Smith, 1987). For smooth obstacles, such as hemispheres and ellipsoids, the dynamics of these arch vortices are governed by two competing mechanisms, the shear flow which advects the vortices and Biot-Savart self induction (Hajimirzaie *et al.*, 2012). When the former dominates, arch vortices tilt downstream and induce upwash at the symmetry plane of the obstacle, forming base vortices (Savory & Toy, 1986*b*; Hajimirzaie *et al.*, 2012); when the latter dominates, arch vortices tilt upstream and induce downwash (Hajimirzaie *et al.*, 2012; Carr & Plesniak, 2016).

The strength of base vortices is strongly influenced by the obstacle aspect ratio and incoming flow boundary layer thickness (Savory & Toy, 1986*b*; Mason & Morton, 1987). With an aspect ratio around 0.25, the strength of the upwash induced by base vortices increases significantly with decreasing boundary layer thickness; for aspect ratios greater than 1, in contrast, the strength of upwash decreases with decreasing boundary layer thickness (Mason & Morton, 1987; Savory & Toy, 1986*b*; Hajimirzaie *et al.*, 2012). An appropriately sized surface obstacle subjected to a laminar boundary layer can act as a flow transition element, wherein flow perturbations induced by the obstacle propagate spanwise, creating a wedge shape with a fully turbulent core bounded by transitional regions, known as a turbulent wedge (Schubauer & Klebanoff, 1955).

The present work compares the flow development over isolated, surface-mounted, 3D obstacles inspired by geometries of droplets deposited on a flat surface in a crossflow. The aim is to characterize the time-averaged flow development over such shapes towards the assessing the aerodynamic loading experienced by droplets under wind-forcing. Furthermore, the influence of different geometries on the propagation of flow perturbations and, consequentially, the laminar-to-turbulent transition process, is explored. Lastly, characteristic frequencies of velocity fluctuations associated

to vortex shedding are investigated.

Research Methodology

Experiments were carried out in the closed-loop wind tunnel ($0.6 \times 0.6\,\mathrm{m}^2$ test section) at the University of Waterloo, which has a free-stream turbulence intensity of less than 0.06%. A flat plate of length 1.5 m and span of 0.6 m was installed in the test section. The leading edge of the flat plate has a super elliptic profile to prevent flow disturbances due to curvature discontinuities. Three solid, surface-mounted models were considered (Fig. 1(a)). A spherical cap was used as a baseline model (referred as 'chopped'). In addition, models representative of a sessile droplet (referred to as 'sessile') and a deformed droplet under wind forcing (referred to as 'runback') were considered, the latter created based on tests of water droplets in boundary layer flows. The 'chopped', 'sessile', and 'runback' models had heights of $h = 7.64$, 7.69, and 7.94 mm and spans of $c = 22.39$, 22.41, and 23.99 mm, respectively. These dimensions correspond to respective aspect ratios of $h/c = 0.341$, 0.343, and 0.331. The models were installed along the plate centerline 735 mm downstream of the leading edge. For the investigated freestream velocity of $U_\infty = 4\,\mathrm{m/s}$, this location corresponds to a Reynolds number of approximately $\mathrm{Re}_h = 2070$ ($\mathrm{Re}_x = 196000$) and boundary layer thickness to height ratio of around $\delta/h = 1$.

Time-resolved planar particle image velocimetry (PIV) was used to capture the instantaneous velocity fields in the $x-y$ plane, see Fig. 1(b) for the coordinate system definition. Illumination was provided by a Photonics DM20-527 Nd-YLF pulsed laser, with a laser sheet thickness of approximately 1 mm. The flow was seeded with water-glycol-based fog with droplets of mean diameter of approximately 1 μm. Two 1024×1024 px Photron SA4 high-speed cameras, each equipped with a Nikon 200 mm lens, were used to capture a combined field of view (FOV) of $85 \times 45\,\mathrm{mm}^2$ (Fig. 1(b)), with a FOV of $45 \times 45\,\mathrm{mm}^2$ for each camera. The numerical aperture and magnification factor were $f_\# = 4$ and $M = 0.455$, respectively. The illumination and imaging system for image acquisition were controlled by a LaVision High-Speed controller and the DaVis 8 program; the latter was also used for image processing. The particle images were acquired in double-frame mode at 1 kHz, with a total of 2560 image pairs collected for each set of experimental conditions. A sequential cross-correlation algorithm with multi-pass iterations of decreasing interrogation window sizes was used to process the images. The final interrogation window was 24×24px with 75% overlap, resulting in a vector pitch of 4 vectors/mm.

Stereoscopic PIV was used to capture dominant three-dimensional attributes of the flow development downstream of the droplet models in a series of $y-z$ planes, see Fig. 1(b). Light provided by an Evergreen 70 Nd-YAG laser was formed into a sheet of 1 mm thickness. The Photron SA4 cameras equipped with the Nikon 200 mm lenses captured the same $45 \times 45\,\mathrm{mm}^2$ FOV. The numerical aperture and magnification factor were $f_\# = 11$ and $M = 0.455$, respectively. The images were acquired in double-frame mode at 15 Hz. A total of 1500 image pairs were collected for each set of experimental conditions. Cross-correlation with multi-pass iterations of decreasing interrogation window sizes was used to process the images. The final interrogation window was 24×24px with 75% overlap, resulting in a vector pitch of 4 vectors/mm.

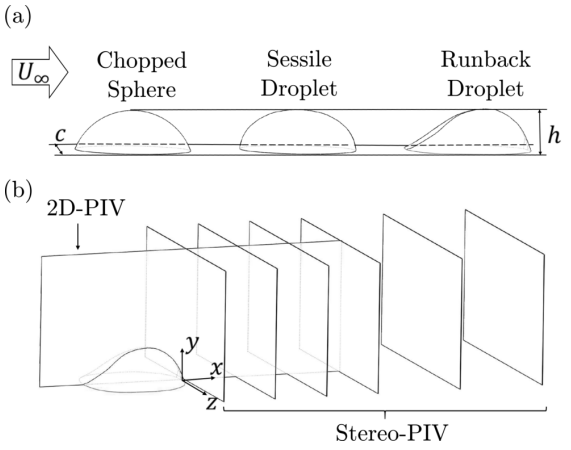

Figure 1. (a) Geometry of models. (b) Fields of view for PIV measurements.

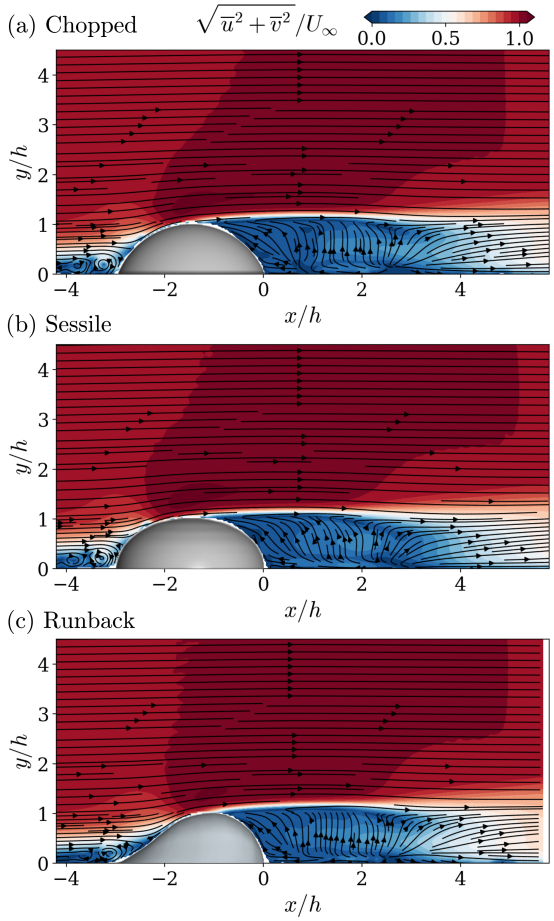

Figure 2. In-plane time-averaged velocity magnitude overlaid with streamlines for the (a) 'chopped', (b) 'sessile', and (c) 'runback' models.

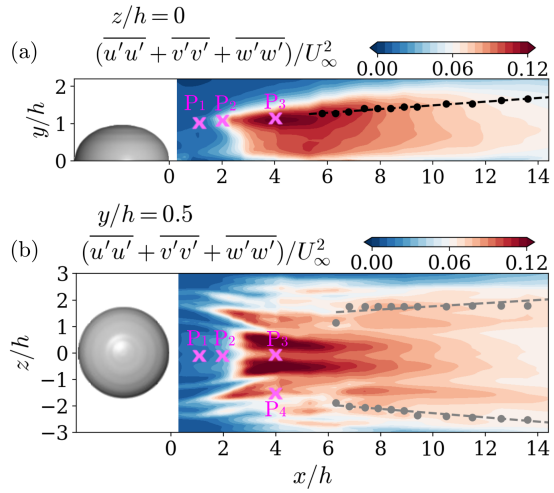

Figure 3. (a) Turbulence kinetic energy in the $x-y$ plane at $z/h = 0$ for the 'sessile' model (black dots: locations of maximum streamwise velocity fluctuations; dashed line: linear fits; magenta crosses: sampling locations for power spectra). (b) Turbulence kinetic energy in the $x-z$ plane at $y/h = 0.5$ for the 'sessile' model (grey dots: projected locations of secondary streamwise velocity fluctuation peaks in the $y-z$ plane; dashed line: linear fits; magenta crosses: projected sampling locations for power spectra).

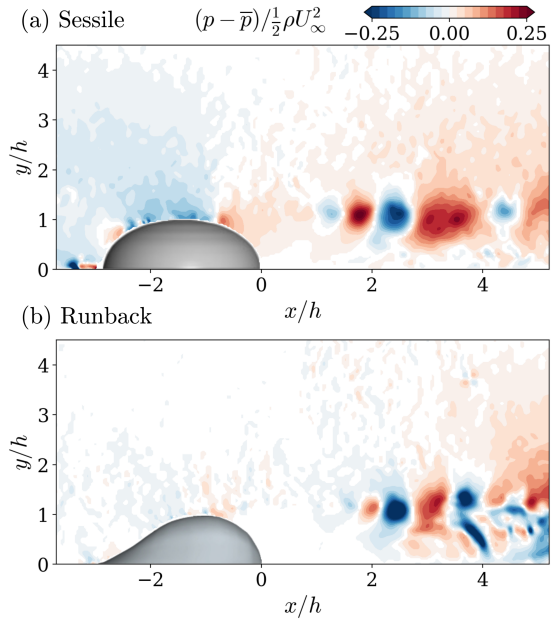

Figure 4. Vortex shedding from the top of (a) 'sessile' and (b) 'runback' models visualized by the pressure fluctuations reconstructed from PIV velocity measurements.

Time-averaged Flow Development

Time-averaged velocity fields in the upstream and near-wake of the obstacles are obtained by averaging TR-PIV measurements over around 12 vortex shedding cycles. Fig. 2 presents contours of the time-averaged velocity magnitude ($\sqrt{\overline{u}^2 + \overline{v}^2}$) at the model symmetry plane overlaid with streamlines in the $x-y$ plane for the three models. As the laminar boundary layer approaches the model, it detaches from the substrate and forms a horseshoe vortex system (Savory & Toy, 1986*b*), part of which is resolved within $-4 < x/h < -3$ in Fig. 2. The separated flow reattaches to the model, forming a stagnation region at $y/h = 0.53$, 0.56, and 0.45 for the 'chopped', 'sessile' and 'runback' models, respectively. The flow separates from the models at around the model maximum height and reattaches to the substrate at $x/h = 2.8$, 3.3, and 2.6 for the three models, respectively. The lengths of the recirculation regions measured from the model maximum height are $x_r/c = 1.4$, 1.6, and 1.3, respectively. Comparable values were reported for cubes (Hussein & Martinuzzi, 1996), hemispheres (Savory & Toy, 1986*b*), cylinders (Pattenden *et al.*, 2002), and ellipsoids (Hajimirzaie *et al.*, 2012) under similar incoming flow conditions.

Fig. 3(a) shows contours of the turbulence kinetic energy on the model symmetry plane for the 'sessile' model. Strong velocity fluctuations develop in the separated shear layer downstream of the model and reach a maximum value just downstream of the mean reattachment location at $x/h \approx 3.5$. This is attributed to the shedding and interaction of the shear layer vortices, as confirmed via time-resolved measurements. Similar results are found for the 'chopped' and 'runback' models, which are omitted here for brevity.

Fig. 4 presents snapshots visualizing the shear layer vortices with local pressure fluctuations reconstructed from in-plane velocity measurements (van Oudheusden, 2013), with negative values marking the vortex cores. For the 'sessile' model shown in Fig. 4(a), vortical structures are clearly visualized in the range $1 < x/h < 4$. A merging event is captured in the range of $3 < x/h < 4$, illustrated by an increase in spacing of successive vortex cores. The shear layer vortices downstream of the model exhibit 'legs' extending upstream towards the substrate, indicating the arch-shaped structures are tilted downstream by the shear flow. This is aligned with the observation by Savory & Toy (1986*b*) and Hajimirzaie *et al.* (2012), which is further confirmed by the vortex imprints in the in the $y-z$ planes, as shown in Fig. 5. For the 'runback' model shown in Fig. 4(b), shear layer vortices form further downstream and are more closely spaced as compared to those of the 'sessile' model.

As shown in Fig. 5(a-1), directly downstream of the 'sessile' model, vortices of alternate signs are observed symmetrical to the model symmetry plane, visualizing the imprint of the horseshoe vortex system. The weak streamwise vorticity in the centre is attributed to the initial tilting of the arch vortex shed from model surface. Moving downstream, the arch vortex is tilted downstream by the shear flow, forming a base vortex pair, which induces upwash at the symmetry plane. At $x/h = 2.7$ (Fig. 5(a-2)), close to the mean flow reattachment location along the centreline, vortex lines of the base vortices curve inward with the free shear layer, maximizing the central upwash. The maximum upwash velocities induced by the 'chopped', 'sessile', and 'runback' models are $v/U_\infty = 0.29$, 0.21, and 0.33, respectively, which are inversely related to the model aspect ratio and recirculation region lengths. A secondary wall vortex pair is induced below the base vortex pair as the streamwise vorticity increases in the base vortices due to further tilting of the arch vortex. Horseshoe vortices of the same sign orbit around each other due to mutually induced velocity, leading to vortex stretching and merging in the $y-z$ plane, in the region of $1.5 \leq |z|/h \leq 2.5$. The interactions of the

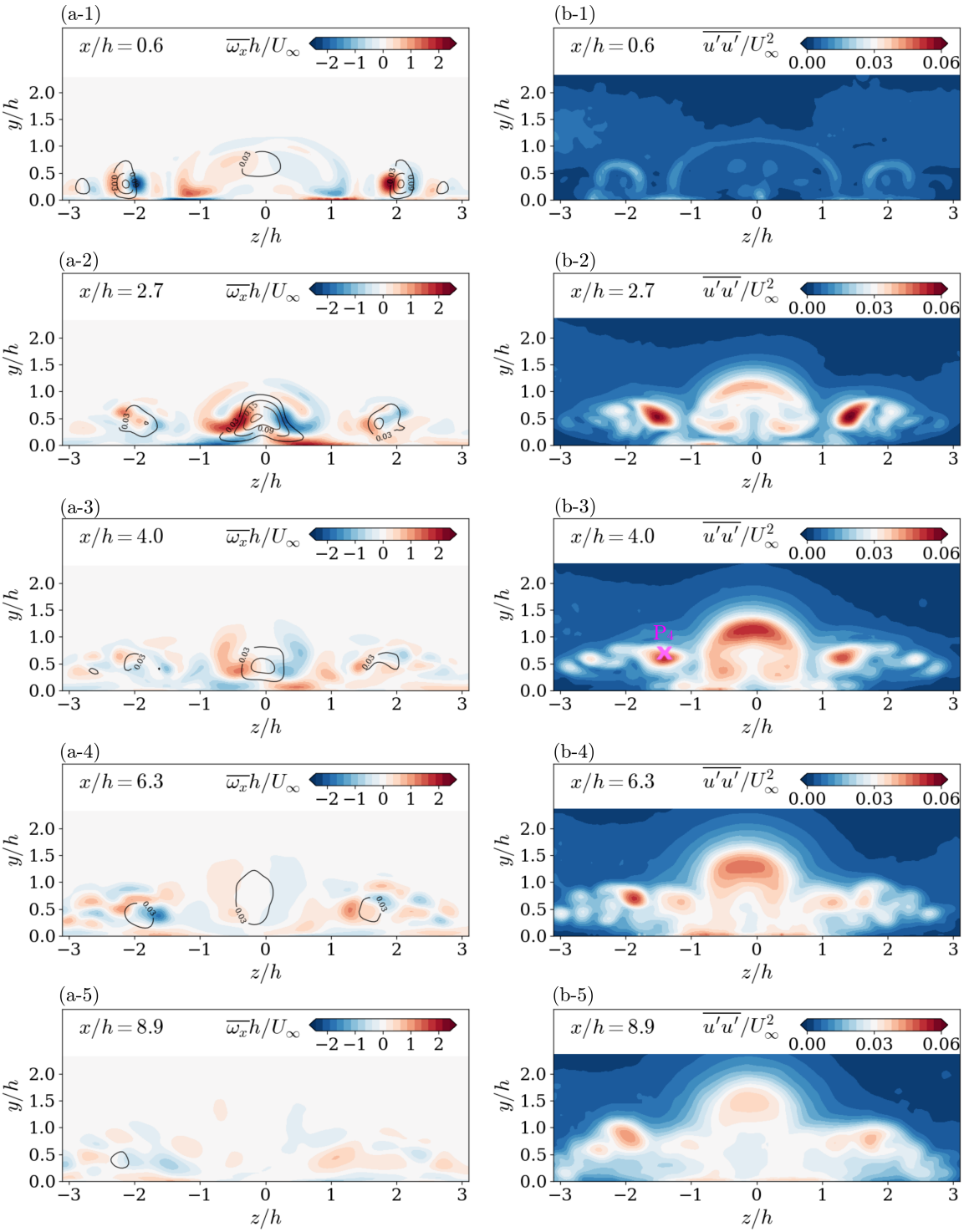

Figure 5. Streamwise vorticity (left column, a-1 to a-5) and mean square of streamwise velocity fluctuations (right-column, b-1 to b-5) in the wake of the 'sessile' model for the $y-z$ planes at (row 1) $x/h = 0.6$, (row 2) $x/h = 2.7$, (row 3) $x/h = 4.0$, (row 4) $x/h = 6.3$, and (row 5) $x/h = 8.9$ in the wake of the 'sessile' model. Solid lines: positive wall-normal velocity.

horseshoe vortices lead to strong streamwise fluctuations at around $x/h = \pm 1.5$ (Fig. 5(b-2)).

By $x/h = 4.0$, the remnant of horseshoe vortex system interacts with the base vortex pair and its induced wall vortices via a similar mechanism (Fig. 5(a-3)). Strong streamwise velocity fluctuations are also observed in the $y-z$ plane near the middle of the model due to the merging of shear layer vortices, aligned with the observation made in the $x-y$ plane (Fig. 5(b-3)). Further downstream, the horseshoe vortex system, base vortices, and induced wall vortices lose coherence resulting from vortex breakdown and mutual annihilation (Fig. 5(a-4)). This produces a turbulent wedge starting at around $x/h = 6$, marking the final stage of transition to turbulence. Two peaks of streamwise velocity fluctuations on both sides of the symmetry plane at around $z/h = \pm 1.8$ mark the boundary of the turbulent wedge (Fig. 5(b-4)). These peaks sustain the cascade of velocity fluctuations and advance laminar-to-turbulent tran-

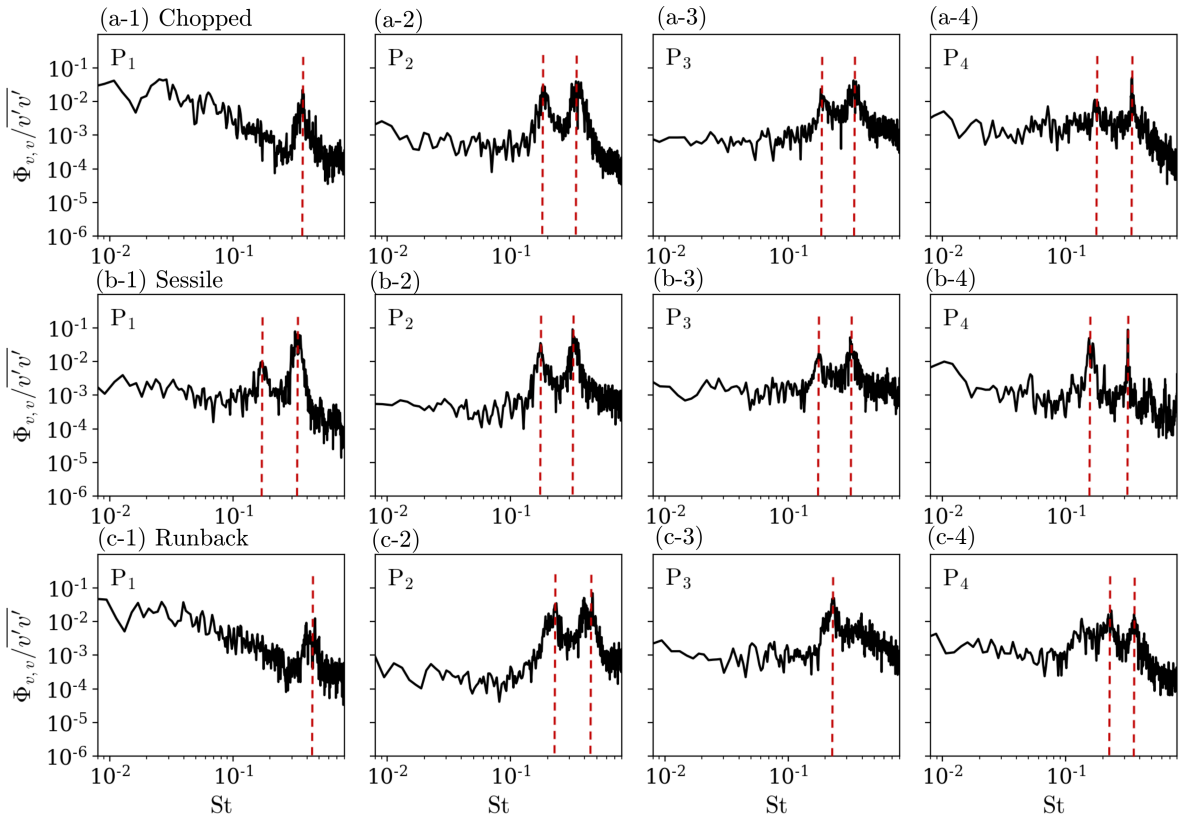

Figure 6. Power spectra of wall-normal velocity fluctuations for (a) 'chopped', (b) 'sessile', and (c) 'runback' models at 4 sampling locations marked in Figs. 3 and 5(b-3).

sition to the laminar flow surrounding the turbulent wedge (Ye *et al.*, 2016). At $x/h = 8.9$, the imprints of the horseshoe vortex system, the base vortex pair and the induced secondary wall vortices are not distinguishable (Fig. 5(a-5)), while the disturbances introduced by the presence of the obstacle propagate sidewards (Fig. 5(b-5)).

The propagation of velocity perturbations in the turbulent wedge is characterized by the wall-normal and spanwise growth of the wake, as shown in Fig. 3. The black dots in Fig. 3(a) mark the locations of maximum $\overline{u'u'}$ values identified in the shear layer on the $x-y$ plane; those in Fig. 3(b) mark the projected locations of $\overline{u'u'}$ peaks identified on each $y-z$ plane onto the $x-z$ plane at the model half-height ($y/h = 0.5$). Wall-normal growth rate and spreading half-angle of the turbulent wedge is evaluated from the slope of the dashed lines fitting through the black dots. The 'sessile' and 'runback' models exhibit spreading half-angles of 4.0° and 4.6°, respectively. The latter is in fair agreement with the value reported for microramps (Ye *et al.*, 2016). The 'chopped' model exhibits a higher spreading half-angle of 7.9°. The wall-normal growth rate for the 'chopped', 'sessile' and 'runback' models are $\mathrm{d}y/\mathrm{d}x = 0.033$, 0.049, and 0.035, respectively, and are inversely related to the spanwise spreading angles.

Characteristic Frequencies

The mean flow topology indicates that shedding and convection of arch vortices profoundly influence the development of the near-wake. The periodic nature of these arch vortices, formed due to shear layer instability, is clearly illustrated in Fig. 4. Characteristic frequencies of the velocity fluctuations induced by these coherent structures are investigated at several locations, P_1 - P_4, in the near wake. P_1, P_2, and P_3 are sampled along the shear layer in the $x-y$ plane at $x/h = 1$, 2, and 4, respectively, as shown by magenta crosses in Fig. 3; P_4 is offset from the model symmetry plane by approximately $1.5h$, corresponding to the $\overline{u'u'}$ peak in the $y-z$ plane at around $x/h = 4$, as shown by magenta cross in Fig. 5(b-3).

Fig. 6 presents spectra of wall-normal velocity fluctuations at P_1 - P_4, with the Strouhal number defined as $\mathrm{St} = fh/U_\infty$. For the 'chopped' model, at P_1, a primary peak centred around $\mathrm{St}_1 = 0.36$ dominates the velocity fluctuations (Fig. 6(a-1)). Going downstream along the shear layer at the symmetry plane, a secondary peak, centred around $\mathrm{St}_2 = 0.18$, emerges at $x/h \approx 1.5$ and reaches comparable magnitude as the primary peak at P_2. This is attributed to periodic vortex merging taking place in this region. Further downstream at P_3, the magnitudes of both peaks diminish, while the energy contained at higher frequencies increases, indicating energy cascading from large vortical structures to small eddies in the process of laminar-to-turbulent transition. At P_4, there exists a peak at around St_1, but there is no significant peak at St_2. This indicates that merging events are less significant for the legs of arch vortices as compared to the head.

For the 'sessile' model, at P_1, velocity fluctuations exhibit a primary peak around $\mathrm{St}_1 = 0.34$, and a weaker secondary peak around $\mathrm{St}_1 = 0.17$. This indicates merging events of shear layer vortices occur earlier upstream as compared to those of the 'chopped' model. Similar to the case of the 'chopped' model, the magnitudes of the two peaks become comparable at P_2 and diminish at P_3. At the span-

wise location P_4, peaks of comparable magnitudes centred around St_1 and St_2 are observed. This indicates that vortex merging involves the legs as well as the heads of the arch vortices in this region.

For the 'runback' model, at P_1, a primary peak of a higher Strouhal number of around $St_1 = 0.42$ is observed, as compared to that of the 'chopped' and 'sessile' models. Similar to the 'chopped' model, at P_2, the velocity fluctuations exhibit a secondary peak of comparable magnitude as the primary peak centered around $St_2 = 0.23$. However, further downstream at P_3, the primary peak no longer appears in the spectrum, and the velocity fluctuations are dominated by the secondary peak. This indicates the heads of arch vortices experience merging to a larger extent until $x/h = 4$. At the spanwise location, P_4, apart from a peak observed at St_1, velocity fluctuations exhibit a broad peak around St_2 and its subharmonics. This indicates that triple merging of the arch vortex legs occurs in this region.

Characteristic Strouhal numbers reported by previous studies range from 0.23 to 0.44 as Re_h increases from 225 to 800 for surface-mounted hemispheres submerged in laminar boundary layers (Savory & Toy, 1986*a*). For hemispheres submerged in turbulent boundary layers, the Strouhal number drops from $St = 0.14$ for $Re_h = 2.5 \times 10^4$ (Wood *et al.*, 2016) to 0.08 for $Re_h = 6 \times 10^4$ (Fedrizzi *et al.*, 2012). The characteristic Strouhal numbers found in the present study ($Re_h = 2070$) are in fair agreement with the values reported for hemispheres submerged in laminar boundary layers.

Conclusions

Flow development of a laminar boundary layer under the influence of isolated surface-mounted, 3D obstacles of droplet inspired geometries ('chopped', 'sessile', and 'runback') is investigated using PIV, with boundary layer thickness $\delta/h = 1$ and model height-based Reynolds number $Re_h = 2070$. Upstream of the model, the flow separates from the substrate and rolls up to form a horseshoe vortex system necklacing around the model. Along the model surface, flow separates at the maximum height location and reattaches back to the substrate downstream, forming a recirculating region. Periodic shedding of arch-shaped structures is observed in the near wake due to the amplification of instabilities in the separated shear layer. Tilting of these arch vortices due to the shear flow forms base vortices, inducing upwash at the model symmetry plane.

In the near wake, the mean flow topology is largely influenced by the aspect ratios of the models, with the lengths of recirculating regions being directly related and the maximum central upwash inversely related to the model aspect ratio. The shedding frequencies of the arch vortices are found to be inversely related to the model aspect ratio, with $St_1 = 0.36$, 0.34, and $0,42$ for the 'chopped', 'sessile', and 'runback' models, respectively. Moving downstream, the mutual annihilation and breakdown of horseshoe vortices and base vortices cascade kinetic energy to smaller eddies, initializing the last stages of laminar-to-turbulent transition. In the far wake, as the boundary layer perturbations induced by the obstacles propagate outward, the turbulent-non-turbulent interfaces exhibit a wedge shape. The spreading half-angles are 7.9°, 4.0°, and 4.6° for the 'chopped', 'sessile', and 'runback' models, respectively.

Acknowledgment

The authors gratefully acknowledge the Natural Sciences and Engineering Research Council of Canada (NSERC), Ontario Centres of Excellence, and Suncor Energy for funding this work.

REFERENCES

Acarlar, MS & Smith, CR 1987 A study of hairpin vortices in a laminar boundary layer. part 1. hairpin vortices generated by a hemisphere protuberance. *Journal of Fluid Mechanics* **175**, 1–41.

Antonini, C, Amirfazli, A & Marengo, M 2012 Drop impact and wettability: From hydrophilic to superhydrophobic surfaces. *Physics of fluids* **24** (10), 102104.

Carr, IA & Plesniak, MW 2016 Three-dimensional flow separation over a surface-mounted hemisphere in pulsatile flow. *Experiments in Fluids* **57** (1), 9.

Fedrizzi, M, Giacobello, M, Soria, J, Atkinson, C & Jones, M 2012 Experimental investigation of a hemisphere in a thin flat plate boundary layer. *no. December* pp. 18–21.

Hajimirzaie, SM, Wojcik, CJ & Buchholz, JHJ 2012 The role of shape and relative submergence on the structure of wakes of low-aspect-ratio wall-mounted bodies. *Experiments in fluids* **53** (6), 1943–1962.

Hansman, RJ & Turnock, SR 1989 Investigation of surface water behavior during glaze ice accretion. *Journal of Aircraft* **26** (2), 140–147.

Hussein, HJA & Martinuzzi, RJ 1996 Energy balance for turbulent flow around a surface mounted cube placed in a channel. *Physics of Fluids* **8** (3), 764–780.

Mason, PJ & Morton, BR 1987 Trailing vortices in the wakes of surface-mounted obstacles. *Journal of Fluid Mechanics* **175**, 247–293.

van Oudheusden, BW 2013 PIV-based pressure measurement. *Measurement Science and Technology* **24** (3), 032001.

Pattenden, RJ, Turnock, SR & Bressloff, NW 2002 An experimental and computational study of 3-d unsteady flow features found behind a cylinder. In *Third Fluids Engineering Summer Meeting, Japan*.

Savory, E & Toy, N 1986*a* The flow regime in the turbulent near wake of a hemisphere. *Experiments in Fluids* **4** (4), 181–188.

Savory, E & Toy, N 1986*b* Hemisphere and hemisphere-cylinders in turbulent boundary layers. *Journal of Wind Engineering and Industrial Aerodynamics* **23**, 345–364.

Schubauer, GB & Klebanoff, PS 1955 Contributions on the mechanics of boundary-layer transition. *NACA-TR-1289* .

Wood, JN, de Nayer, G, Schmidt, S & Breuer, M 2016 Experimental investigation and large-eddy simulation of the turbulent flow past a smooth and rigid hemisphere. *Flow, Turbulence and Combustion* **97**, 79–119.

Ye, Q, Schrijer, FFJ & Scarano, F 2016 Geometry effect of isolated roughness on boundary layer transition investigated by tomographic piv. *International Journal of Heat and Fluid Flow* **61**, 31–44.